Finite-volume lattice Boltzmann schemes in two and three dimensions

Haowen Xi,[1] Gongwen Peng,[2] and So-Hsiang Chou[3]
[1]*Department of Physics and Astronomy, Bowling Green State University, Bowling Green, Ohio 43403*
[2]*Department of Chemical and Petroleum Engineering, University of Pittsburgh, Pittsburgh, Pennsylvania 15261*
[3]*Department of Mathematics and Statistics, Bowling Green State University, Bowling Green, Ohio 43403*
(Received 3 March 1999; revised manuscript received 7 April 1999)

Simple and practical finite-volume schemes for the lattice Boltzmann equation are derived in two and three dimensions through the application of modern finite-volume methods. The schemes use a finite-volume vortex-type formulation based on quadrilateral elements in two dimensions and trilinear hexahedral elements in three dimensions. It is shown that the schemes are applicable to domains with irregular boundaries of arbitrary shape in two and three dimensions. [S1063-651X(99)10809-2]

PACS number(s): 47.11.+j, 05.20.Dd, 47.10.+g

I. INTRODUCTION

In the past ten years, there has been steadily increasing interest in the lattice Boltzmann method (LBM) as a novel approach for solving the fluid dynamics problems. This is due to the fact that the LBM has some very attractive features such as inherent parallelism, simplicity of coding, and capability of incorporating complex geometry and microscopic interactions in multiphase fluids [1–4].

However, if one compares the LBM with the state-of-the-art computational-fluid-dynamics (CFD) techniques, one finds that the LBM still has some shortcomings. One of these is that the LBM is restricted on a special class of uniform and regular spatial lattices. The limitation of using uniform lattices is particularly severe in many practical applications where the complex geometry of boundaries cannot be well fitted by regular lattices. This is in contrast with the modern CFD techniques, which are generally capable of accommodating fairly complex spatial meshes. Motivated by such considerations, several researchers have attempted to extend the applicability of the LBM to irregular lattices. Succi and his collaborators [5] were the first to propose a finite-volume formulation of the lattice Boltzmann equation (LBE). However, the empirical formulas are quite complicated even for the simple rectangular meshes, and a free parameter has to be introduced and adjusted in order to minimize the numerical diffusion. Quite recently, another elegant finite-volume scheme was developed by Chen [6]. In another approach proposed by He, Luo, and Dembo [7] for an arbitrary rectangular mesh, the density distributions move along their respective directions of velocities to points which may or may not be on grid points. An interpolation step is thus introduced to determine the density distributions at the grid points for the next time step. However, the above-mentioned approaches of using irregular meshes are not satisfactory in the sense that the topology of the meshes used in the proposed models is not arbitrary. In recent papers [8,9] we have proposed a new scheme based on modern finite-volume methods [10,11] which is applicable to irregular meshes with arbitrary connectivity. While our methods follow from an application of finite-volume methods to the LBE, they still keep much of the simplicity of the conventional LBM. In this paper, we are going to give a detailed account of the quadrilateral scheme and validate it through extensive simulations.

Though successful in two dimensions, our 2D scheme still cannot deal with the realistic fluid flows which are usually three-dimensional problems. In this paper, we are also going to present a three-dimensional (3D) scheme. In order to be a practical scheme, a new scheme should be simple enough in three dimensions and easy enough to code. We believe that our scheme satisfies these requirements. And after all, our scheme is accurate, a point which will be proven by comparing the numerical results with analytical ones. Designing a 3D scheme is a nontrivial work. A great deal of care has to be taken in order to create a simple and practical scheme. In what follows, one can see that our model for the hexahedral elements looks as if the interpolation *were* linear. In fact, it is not linear but cubic in nature. This feature is remarkable and is indeed a product of achieving the goal of designing an easy-to-use, practical scheme while maintaining accuracy.

To appreciate the modern CFD techniques, one has to begin with grid (or mesh) generation for the physical domain. There are two general types of grids commonly used in the modern CFD for discretizing the domain: structured grids and unstructured grids. A structured grid is an i-j-ordered array of points in two dimensions and an i-j-k-ordered array of points in three dimensions. Topologically and computationally, the structured grid is still rectangular. An unstructured grid, often used in finite-element computations, is an array of points with no particular logical order. It offers more flexibility in representing complex geometries. However, this flexibility does not come without a price. The spatial relationship between one grid and the others must be explicitly stated since there is no logical relationship between one grid and its neighbors in their indexes. Thus the computational speed with unstructured grids is often reduced compared with using structured ones. Thanks to the recent development of grid generation techniques [12,13], the structured grids can now be generated over the entire physical domain with very complex shape. Although our finite-volume schemes are applicable to both structured and unstructured grids with arbitrary connectivity, in this paper we will focus on presenting the explicit finite-volume schemes in structured grids.

Grids can be constructed from a variety of finite elements. One often uses a set of triangular elements (usually for unstructured grids) or quadrilateral elements (often for struc-

tured grids) in two dimensions, and tetrahedra elements (usually for unstructured grids) or hexahedra elements (often for structured grids) in three dimensions. The size and shape of the element can be varied to place more elements as one wishes in an area of interest. It is important to distinguish the difference between finite elements and grids: Grids are the numerical nodes in the physical domain, while finite elements are the basic geometric structures covering the domain. Thus, one can have structured grids with triangular elements (e.g., a simple regular triangular lattice with six neighbors around each node), and one can also have unstructured grids with triangular elements (e.g., an irregular triangular mesh with different number of neighbors around different nodes). In what follows, the formulations of our finite-volume methods for the lattice Boltzmann equation with quadrilateral and hexahedral elements are given in Sec. II and Sec. III, respectively; numerical simulation results on various fluid problems are presented in Sec. IV, and Sec. V concludes with a discussion and summary.

II. FINITE-VOLUME LATTICE BOLTZMANN SCHEME IN TWO DIMENSIONS

In the original formulations of the LBM it was understood that the discretization of velocity space is closely coupled to that of physical space. For example, one model commonly used is the nine discrete velocities in association with the square lattice in physical space in two dimensions. Similarly for a triangular spatial lattice, the seven discrete velocities were used. But as discovered in recent papers [7,14,15], this coupling is actually not necessary. The discretizations in velocity space and in physical space can be treated independently in general. Our starting point of this paper is the lattice Boltzmann equation (LBE). Recently, it was shown [16] that the LBE can be directly derived from the Boltzmann equation by discretization of velocity space, giving a solid root to the LBE. General finite-difference discretizations of the LBE can be found in Ref. [15].

In the following, we present our finite-volume lattice Boltzmann method (FVLBM) with quadrilateral elements in two dimensions. We start with the lattice Boltzmann equation, which reads:

$$\frac{\partial f_i}{\partial t}+\mathbf{v}_i\cdot\boldsymbol{\nabla} f_i=\Omega_i+\alpha\mathbf{v}_i\cdot\mathbf{F}, \tag{1}$$

where f_i is the particle distribution function associated with motion along the ith direction in velocity space, $\mathbf{v}_i$ is the velocity in the ith direction, $i=1,2,\ldots,m$ with m the number of different velocities in the model, $\mathbf{F}$ is the external body force, coefficient $\alpha=1/\Sigma_i v_{ix}^2=1/\Sigma_i v_{iy}^2$, and Ω_i is the collision operator commonly approximated by the Bhatragar-Gross-Krook model [17], or the single-time relaxation approximation,

$$\Omega_i=-\frac{1}{\tau}(f_i-f_i^{\mathrm{eq}}), \tag{2}$$

where f_i^{eq} is the local equilibrium distribution and τ is the relaxation time. Here we will choose the nine velocities-bit (D2Q9—two dimensions, nine velocities) model [18] for the velocity discretization and arbitrary quadrilateral element for the spatial discretization. The nine discrete velocities are defined by

$$\mathbf{v}_i=\begin{cases}(0,0), & i=0\\ (\cos[(i-1)\pi/2],\sin[(i-1)\pi/2]), & i=1,2,3,4\\ \sqrt{2}(\cos[(i-5)\pi/2+\pi/4],\sin[(i-5)\pi/2+\pi/4]), & i=5,6,7,8\end{cases} \tag{3}$$

and the equilibrium distribution f_i^{eq} is given by [18]

$$f_i^{\mathrm{eq}}=w_i\rho[1+\tfrac{3}{2}(\mathbf{v}_i\cdot\mathbf{u})+\tfrac{9}{2}(\mathbf{v}_i\cdot\mathbf{u})^2-\tfrac{3}{2}|\mathbf{u}|^2], \tag{4}$$

where

$$\rho=\sum_i f_i, \tag{5}$$

$$\mathbf{u}=\sum_i f_i\mathbf{v}_i/\rho \tag{6}$$

are the density and velocity, respectively, and

$$w_i=\begin{cases}4/9, & i=0\\ 1/9, & i=1,2,3,4\\ 1/36, & i=5,6,7,8.\end{cases} \tag{7}$$

The equilibrium distribution is formulated specifically to recover the Navier-Stokes equation in the low-Mach-number limit with kinematic viscosity $\nu=\tau/3$ [14,15].

In order to solve the above LBE [Eq. (1)], one could use one of two common methods: the finite-difference method and the finite-volume method. In the finite-difference approach, the differential form of the equation is solved at discrete space points. On the other hand, the finite-volume approach solves an integral form of the equation. Instead of solving the equation at discrete points, the equation is solved over a small ''control volume.'' The finite-volume approach has two major advantages over the finite-difference approach in some area: the integral form of the equation can capture discontinuities in the solution, and it is more suitable for complex geometry. In the following we illustrate how our finite-volume scheme is constructed.

Figure 1(a) shows a generic situation in which quadrilateral elements surround an interior node of the grid. Here we use the finite-volume method of cell-vertex type. In this type of formulation, all f_i's at the grid nodes are known. We need

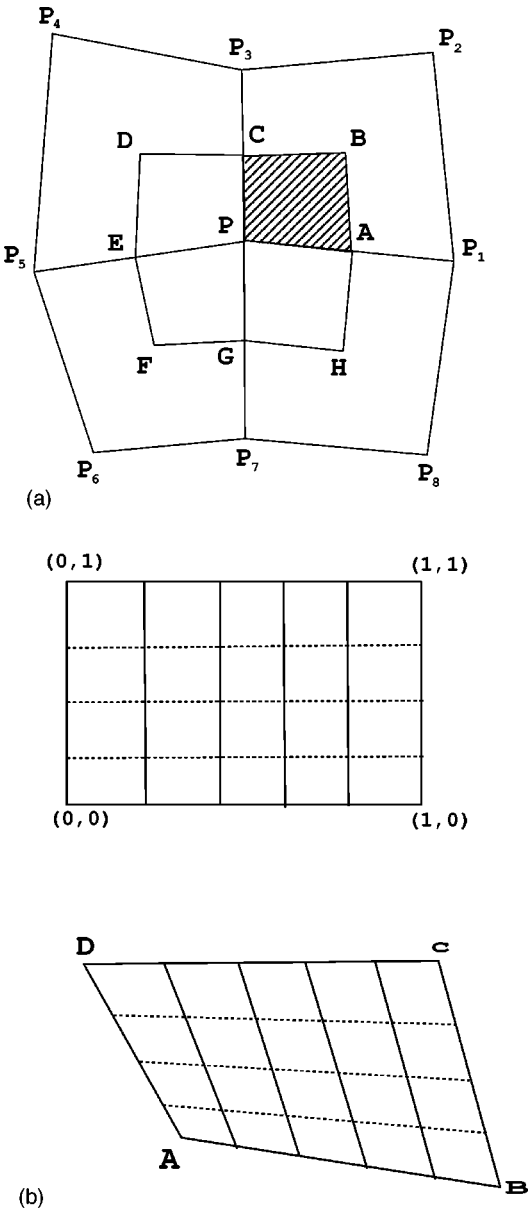

FIG. 1. (a) Diagram of finite elements sharing one common node. Here $P,P_1,P_2,\ldots,P_8$ stand for the mesh grid points. A,B,C,D,E,F,G,H make the edges of the control volume (polygon) over which integration of the PDE of Eq. (1) is performed; (b) diagram for mapping between a unit quadrilateral (upper part) and a general one (lower part).

to calculate the f_i's at non-grid-node positions. These f_i values at non-grid-node positions would be interpolated from the known f_i's at the grid nodes using standard interpolation procedures depending on the type of elements. Let us briefly describe how the interpolation is done in the case of quadrilateral elements. Suppose that the fluid domain is decomposed into a union of quadrilaterals. Furthermore, we assume that if any two quadrilaterals intersect, the intersection can only be their common edge. Each quadrilateral can be viewed as the one-to-one image of the unit square via a coordinate transformation. More specifically, in Fig. 1(b) the bottom quadrilateral Q in the xy plane has vertices A, B, C, and D. There is a unique bilinear mapping of the top unit square $\hat{Q}$ in the $\xi\eta$ plane onto Q:

$$x(\xi,\eta)=x_A+(x_B-x_A)\xi+(x_D-x_A)\eta+(x_C-x_A-x_D-x_A)\xi\eta, \tag{8}$$

$$y(\xi,\eta)=y_A+(y_B-y_A)\xi+(y_D-y_A)\eta+(y_C-y_A-y_D-y_A)\xi\eta. \tag{9}$$

This mapping maps $(0,0),(1,0),(1,1),(0,1)$ to A,B,C,D, respectively, and the straight coordinate lines in the $\xi\eta$ plane to the straight lines in the xy plane as shown in Fig. 1(b). The particle distribution function f_i is then assumed to be linear along the images of either a ξ or η line in the xy plane. Notice that f_i is not bilinear in the x and y variables, but in the ξ and η variables. This is the familiar so-called isoparametric representation commonly used in the finite-element method (see Ref. [10]).

We use the bilinear interpolation to obtain the function value at any position from the values at the four nodes. By ''bilinear'' we mean that a function on a *unit* quadrilateral element $[0\leqslant\xi\leqslant1,0\leqslant\eta\leqslant1]$ has the form of $f(\xi,\eta)=a_0+a_1\xi+a_2\eta+a_3\xi\eta$, where a_0 to a_3 are determined by the function values at the four nodes. Thus the function is linear along constant ξ or η lines. For any quadrilateral element other than a unit quadrilateral element, a mapping should be first used to transfer the element on the xy plane into a unit on the $\xi\eta$ plane, and therefore the function on a general quadrilateral element typically has terms including all quadratic terms of x^2, y^2, and xy. It should be noted that the function is linear along the images of constant ξ and η lines.

We choose the control volume to be the polygon ABCDEFGH surrounding the grid node P as shown in Fig. 1(a). Here A is the midpoint of edge PP_1, C is the midpoint of edge PP_3, and B is the geometric center of element $PP_1P_2P_3$. Thus, the coordinates $\mathbf{x}_A$, $\mathbf{x}_B$, and $\mathbf{x}_C$ are given by

$$\mathbf{x}_A=(\mathbf{x}_P+\mathbf{x}_{P_1})/2,\quad \mathbf{x}_B=(\mathbf{x}_P+\mathbf{x}_{P_1}+\mathbf{x}_{P_2}+\mathbf{x}_{P_3})/4,$$

$$\mathbf{x}_C=(\mathbf{x}_P+\mathbf{x}_{P_3})/2. \tag{10}$$

Likewise, D is the center of element $PP_3P_4P_5$. The integration control volume consists of polygon $PABC$, $PCDE$, $PEFG$, and $PGHA$. In the following we focus on the integration over the polygon $PABC$. Similar integrations would be done over all other polygons and the results summed.

The integration of the first term in Eq. (1) is approximated as

$$\int_{PABC}\frac{\partial f_i}{\partial t}d\sigma=\frac{\partial f_i(P)}{\partial t}S_{PABC}, \tag{11}$$

where S_{PABC} is the area of $PABC$ and $f_i(P)$ is the f_i value at grid node P. In what follows, the grid-node index is given in parentheses following the f_i values. In the above equation, we have made an approximation that f_i is constant over the area $PABC$ to prevent us from having to solve a set of equations. This kind of approximation known as ''lumping'' is a common practice used in the finite-volume methods [11].

The integration of the second term of Eq. (1) will give fluxes through the four edges PA, AB, BC, and CP. Since we will sum over all the polygons like $PABC$, $PCDE$,

$PEFG$, and $PGHA$, the net flux through internal edges (PA, PC, PE, and PG) will cancel out. Therefore, we will omit the explicit expression from the internal edges,

$$\int_{PABC} \mathbf{v}_i \cdot \nabla f_i \, d\sigma = \mathbf{v}_i \cdot \int_{AB} f_i \, d\mathbf{l} + \mathbf{v}_i \cdot \int_{BC} f_i \, d\mathbf{l} + I_s, \quad (12)$$

where I_s represents fluxes through internal edges. With the standard assumption of bilinearity of f_i's in quadrilateral elements, the flux is then given by

$$\int_{PABC} \mathbf{v}_i \cdot \nabla f_i \, d\sigma = \mathbf{v}_i \cdot \mathbf{n}_{AB} l_{AB} [f_i(A) + f_i(B)]/2 + \mathbf{v}_i \cdot \mathbf{n}_{BC} l_{BC} [f_i(B) + f_i(C)]/2 + I_s, \quad (13)$$

where $\mathbf{n}_{AB}$ and $\mathbf{n}_{BC}$ are the unit vectors normal to the edge AB and BC, respectively, and l_{AB} and l_{BC} are the lengths of AB and BC, respectively.

With the assumption of bilinearity of f_i and f_i^{eq} over the quadrilateral elements, the integration over the collision term of Eq. (1) [i.e., Eq. (2)] results in the following formula:

$$-\int_{PABC} \frac{1}{\tau}(f_i - f_i^{\mathrm{eq}}) d\sigma = -\frac{S_{PABC}}{\tau} [\Delta f_i(P) + \Delta f_i(A) + \Delta f_i(B) + \Delta f_i(C)]/4, \quad (14)$$

where

$$\Delta f_i(P) = f_i(P) - f_i^{\mathrm{eq}}(P), \quad (15)$$

$$\Delta f_i(A) = f_i(A) - f_i^{\mathrm{eq}}(A), \quad (16)$$

$$\Delta f_i(B) = f_i(B) - f_i^{\mathrm{eq}}(B), \quad (17)$$

$$\Delta f_i(C) = f_i(C) - f_i^{\mathrm{eq}}(C). \quad (18)$$

Here $f_i(A)$, $f_i(B)$, $f_i(C)$ and their corresponding equilibrium particle distribution $f_i^{\mathrm{eq}}(A)$, $f_i^{\mathrm{eq}}(B)$, $f_i^{\mathrm{eq}}(C)$ functions are the values at nongrid nodes A, B, and C, respectively. These may be obtained by interpolation from the four grid nodes at element $PP_1P_2P_3$,

$$f_i(A) = [f_i(P) + f_i(P_1)]/2, \quad (19)$$

$$f_i(B) = [f_i(P) + f_i(P_1) + f_i(P_2) + f_i(P_3)]/4, \quad (20)$$

$$f_i(C) = [f_i(P) + f_i(P_3)]/2, \quad (21)$$

$$f_i^{\mathrm{eq}}(A) = [f_i^{\mathrm{eq}}(P) + f_i^{\mathrm{eq}}(P_1)]/2, \quad (22)$$

$$f_i^{\mathrm{eq}}(B) = [f_i^{\mathrm{eq}}(P) + f_i^{\mathrm{eq}}(P_1) + f_i^{\mathrm{eq}}(P_2) + f_i^{\mathrm{eq}}(P_3)]/4, \quad (23)$$

$$f_i^{\mathrm{eq}}(C) = [f_i^{\mathrm{eq}}(P) + f_i^{\mathrm{eq}}(P_3)]/2. \quad (24)$$

Substituting Eqs. (15)–(24) into Eq. (14), we obtain

$$-\int_{PABC} \frac{1}{\tau}(f_i - f_i^{\mathrm{eq}}) d\sigma = -\frac{S_{PABC}}{\tau} [9\Delta f_i(P) + 3\Delta f_i(P_1) + \Delta f_i(P_2) + 3\Delta f_i(P_3)]/16. \quad (25)$$

With these results, the integration of Eq. (1) over the polygon $PABC$ is complete. The integration over the whole control volume $ABCDEFGH$ is just the sum of contributions from all these terms over different polygons $PABC$, $PCDE$, $PEFG$, and $PGHA$. Therefore, f_i at grid node P is updated as follows:

$$f_i(P, t + \Delta t) = f_i(P, t) + \frac{\Delta t}{S_P} \left(\sum_{\text{around } P} (\text{collisions}) - \sum_{\text{around } P} (\text{fluxes}) \right) + \alpha \mathbf{v}_i \cdot \mathbf{F}, \quad (26)$$

where S_P is the total area of the control volume around grid node P, and ''collisions'' and ''fluxes'' refer, respectively, to the finite-volume-integrated contributions from the collision term and fluxes.

In the finite-volume scheme of cell-vertex type, the update of the f_i's at boundary nodes is similar to that for interior nodes except that at the boundary the corresponding covolumes are half-covolumes [8]. Let us look at Fig. 1(a) again and assume that P_5, P, and P_1 are boundary nodes separating the fluid (upper half) from the lower half. As for the interior fluid nodes, we update f_i's at P by covolume integrals. However, the covolume is now not complete in the 2π directions as the polygons $PEFG$ and $PGHA$ are now not included. This leads to one difference when integrating the second term of Eq. (1) over polygons $PABC$ and $PCDE$. The flux terms over edges PA and EP, which we omitted in the case of interior nodes [i.e., I_s in Eq. (12)] as they were internal fluxes, must now be included in the calculation. They are actually easy to evaluate as shown in Eq. (12) for fluxes over other edges. The velocity of the boundary wall is used when we calculate f_i^{eq} for the boundary nodes using Eq. (4). This is to enforce the nonslip boundary condition.

III. FINITE-VOLUME LATTICE BOLTZMANN SCHEME IN THREE DIMENSIONS

In three dimensions, we choose the nineteen velocities for the velocity discretization as in the D3Q19 model [18]. The equilibrium distribution functions are

$$f_i^{\mathrm{eq}} = \tfrac{1}{3}\rho[1 - \tfrac{3}{2}\mathbf{u}\cdot\mathbf{u}] \quad \text{if} \quad |\mathbf{v}_i|^2 = 0, \quad (27)$$

$$f_i^{\mathrm{eq}} = \tfrac{1}{18}\rho[1 + 3(\mathbf{v}_i\cdot\mathbf{u}) + \tfrac{9}{2}(\mathbf{v}_i\cdot\mathbf{u})^2 - \tfrac{3}{2}\mathbf{u}\cdot\mathbf{u}] \quad \text{if} \quad |\mathbf{v}_i|^2 = 1, \quad (28)$$

$$f_i^{\mathrm{eq}} = \tfrac{1}{36}\rho[1 + 3(\mathbf{v}_i\cdot\mathbf{u}) + \tfrac{9}{2}(\mathbf{v}_i\cdot\mathbf{u})^2 - \tfrac{3}{2}\mathbf{u}\cdot\mathbf{u}] \quad \text{if} \quad |\mathbf{v}_i|^2 = 2, \quad (29)$$

where $\rho = \Sigma_i f_i$ and $\rho\mathbf{u} = \Sigma_i f_i \mathbf{v}_i$ are the macroscopic mass density and momentum density, respectively.

Given a flow domain, we can fit it with a grid made up of hexahedral elements. The unknown f_i's are sought at the vertices (nodes) of the elements labeled as P_i's in Fig. 2. For

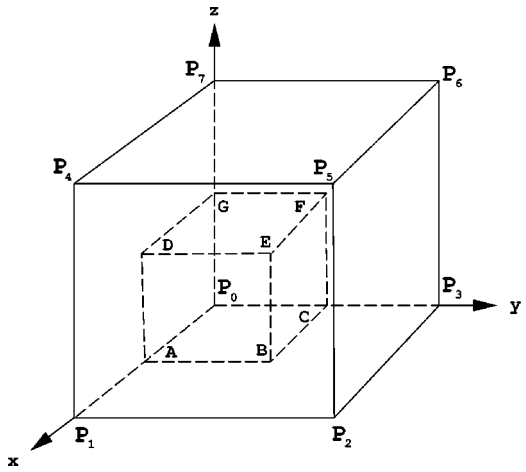

FIG. 2. Diagram of one hexahedral element and its corresponding control volume. Here $P_0, P_1, \ldots,$ and P_7 are the grid nodes.

easy visualization we have drawn the element as a cube. Any interior f_i values are to be computed by interpolating from the f_i's at the nodes using the trilinear interpolation procedures. By trilinear we mean that a function in a *unit* hexahedral element $[0\leqslant\xi\leqslant1,0\leqslant\eta\leqslant1,0\leqslant\chi\leqslant1]$ has the form of $f(\xi,\eta,\chi)=a_0+a_1\xi+a_2\eta+a_3\chi+a_4\xi\eta+a_5\xi\chi+a_6\eta\chi+a_7\xi\eta\chi$, where a_0 to a_7 are determined by the function values at the eight nodes of the hexahedral element. Thus the function is bilinear along constant ξ or η or χ planes, and linear along any axis if the other two are kept constant. For any hexahedral element other than the unit element, a mapping should be first used to transfer the element in xyz space into a unit in $\xi\eta\chi$ space, and therefore the function in a general hexahedral element typically has terms including all cubic terms such as x^3 and x^2y.

In Fig. 2, we are interested in the update of f_i's at node P_0. One could imagine that there are eight hexahedral elements sharing node P_0, though we have only drawn $\frac{1}{8}$ part of them (one hexahedral element) for clear illustration in this figure. The (one-eighth of) control volume at P_0 is chosen as the hexahedron $P_0ABCDEFG$ shown in Fig. 2. Here A, C, and G are the midpoint of edge P_0P_1, P_0P_3, and P_0P_7, respectively, B, D, and F are the geometric center of area element $P_0P_1P_2P_3$, $P_0P_1P_4P_7$, and $P_0P_3P_6P_7$, respectively, and E is the geometric center of volume element $P_0P_1P_2P_3P_4P_5P_6P_7$. In the following, we focus on the integration over the hexahedron $P_0ABCDEFG$. The integration of the first term in Eq. (1) is approximated as

$$\int_{P_0ABCDEFG}\frac{\partial f_i}{\partial t}dv=\frac{\partial f_i(P)}{\partial t}V_{P_0ABCDEFG}, \tag{30}$$

where $V_{P_0ABCDEFG}$ is the volume of hexahedron $P_0ABCDEFG$ and $f_i(P_0)$ is the f_i value at node P_0.

Integration of the second term of Eq. (1) will give fluxes though six surfaces P_0ABC, P_0ADG, P_0CFG, $BCEF$, $ABDE$, and $DEFG$. As in two dimensions, we will omit the fluxes from the internal surfaces. With this, we have

$$\int_{P_0ABCDEFG}\mathbf{v}_i\cdot\nabla f_i\,dv=\mathbf{v}_i\cdot\int_{ABDE}f_i\,d\mathbf{S}+\mathbf{v}_i\cdot\int_{BCEF}f_i\,d\mathbf{S}+\mathbf{v}_i\cdot\int_{DEFG}f_i\,d\mathbf{S}. \tag{31}$$

With the assumption of trilinearity of f_i's in hexahedral elements, the flux is

$$\int_{P_0ABCDEFG}\mathbf{v}_i\cdot\nabla f_i\,dv=I_1+I_2+I_3+I_s \tag{32}$$

with

$$I_1=\mathbf{v}_i\cdot\int_{ABDE}f_i\,d\mathbf{S}=\mathbf{v}_i\cdot\mathbf{n}_{ABDE}S_{ABDE}[f_i(A)+f_i(B)+f_i(D)+f_i(E)]/4, \tag{33}$$

$$I_2=\mathbf{v}_i\cdot\int_{BCEF}f_i\,d\mathbf{S}=\mathbf{v}_i\cdot\mathbf{n}_{BCEF}S_{BCEF}[f_i(B)+f_i(C)+f_i(E)+f_i(F)]/4, \tag{34}$$

$$I_3=\mathbf{v}_i\cdot\int_{DEFG}f_i\,d\mathbf{S}=\mathbf{v}_i\cdot\mathbf{n}_{DEFG}S_{DEFG}[f_i(D)+f_i(E)+f_i(F)+f_i(G)]/4, \tag{35}$$

where $\mathbf{n}_{ABDE}$, $\mathbf{n}_{BCFE}$, and $\mathbf{n}_{DEFG}$ are the unit vectors normal to the surface plane $ABDE$, $BCEF$, and $BCEF$, respectively, and S_{ABDE}, S_{BCEF}, and S_{DEFG} are the areas of surfaces $ABDE$, $BCEF$, and $DEFG$, respectively. $f_i(A), f_i(B), \ldots, f_i(G)$ and their corresponding equilibrium particle distribution functions are the values of these variables at non-node positions $A,B,\ldots,G$. These functions may be obtained by interpolation from the nodes at element $P_0P_1,\ldots,P_7$, e.g., $f_i(A)=[f_i(P_0)+f_i(P_1)]/2$, $f_i(B)=[f_i(P_0)+f_i(P_1)+f_i(P_2)+P_i(P_3)]/4$.

Assuming the trilinearity of f_i and f_i^{eq} over the three-dimensional hexahedral elements, the integration over the collision term of Eq. (1) results in the following formula:

$$-\int_{P_0ABCDEFG}\frac{1}{\tau}(f_i-f_i^{\mathrm{eq}})dv=-\frac{V_{P_0ABCDEFG}}{\tau}\left(\sum_{k=0}^{7}c_k\Delta f_i(P_k)\right), \tag{36}$$

where $\Delta f_i=f_i-f_i^{\mathrm{eq}}$, $c_0=27/64$, $c_1=c_3=c_7=9/64$, $c_2=c_4=c_6=3/64$, and $c_5=1/64$. The $f_i(P_k)$ and their corresponding equilibrium particle distribution functions are the values of these variables at node P_k.

With these results, the integration of Eq. (1) over the $\frac{1}{8}$ control volume, i.e., the hexahedron $P_0ABCDEFG$ centered at node P_0, is complete. The integration over the whole control volume is just the sum of contributions from all these

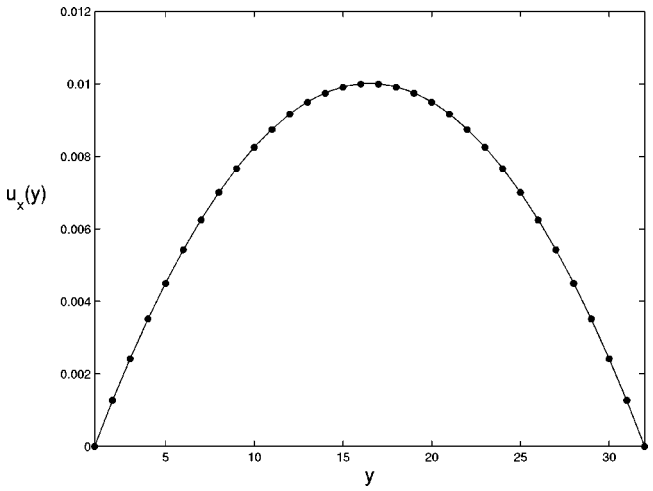

FIG. 3. Numerical velocity profile (data points) in the steady state for the Poiseuille flow compared with the analytical solution (solid curve).

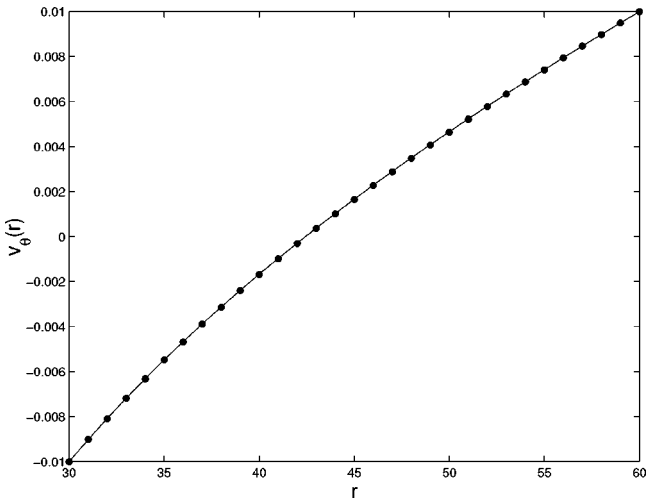

FIG. 4. Numerical velocity profile (data points) in the steady state for rotating Couette flow, compared with the analytical solution (solid curve) $v_\theta(r)=0.01(r/30\text{-}60/r)$.

terms over different hexahedra. Therefore, f_i at node P_0 is updated formally as in Eq. (26), where ''collisions'' and ''fluxes'' are now referring, respectively, to the three-dimensional finite-volume-integrated contributions from the collision term and the fluxes.

IV. NUMERICAL EXAMPLES

In this section, we demonstrate the validity and accuracy of the FVLBM schemes using examples with known exact solutions, or comparing the results with the ones obtained from other traditional methods. The first example is the two-dimensional Poiseuille flow between two parallel plates. We choose the fluid density $\rho=1.0$ and relaxation time $\tau=1.0(\nu=\tau/3=1/3)$ with external body force $\mathbf{F}=2.604\times10^{-5}\mathbf{e}_x$. The numerical parameters for the time and grid steps are $\Delta t=0.5$, $\Delta x=1.0$, and $\Delta y=1.0$. The total $N_x\times N_y=64\times32$ mesh grids are used. We set the initial conditions for the macroscopic velocity field to be zero. Figure 3 shows the numerical results of the steady velocity profile and the corresponding analytical solution $u_x(y)=FL^2/(8\rho\nu)[1-(2y/L-1)^2]$, where $L=\Delta y N_y=32$ is the channel width. The agreement with the theoretical results is excellent, and the global error was found to be $L_1=2.15\times10^{-5}$.

Next, we present two-dimensional simulation of rotating Couette flow where fluid is contained between two concentric cylinders. The outer cylinder rotates with velocity $V_2\mathbf{e}_\theta$, while the inner cylinder rotates with velocity $V_1\mathbf{e}_\theta$, i.e., $v_\theta(r=R_1)=V_1$ and $v_\theta(r=R_2)=V_2$. The important point to note here is that this particular problem possesses high symmetry for flow field, however the FVLBM scheme reported here needs no preassumptions of symmetry. Here we have taken the radii of the two cylinders to be $R_1=30$ and $R_2=60$, the velocity of the inner cylinder $V_1=-0.01$, and the outer cylinder $V_2=0.01$. The numerical parameters for the FVLBM are $\rho=1.0$, $\tau=0.5$, $\Delta t=0.25$, $\Delta\theta=2\pi/180$, and $\Delta r=1.0$. The $N_\theta\times N_r=180\times30$ mesh grids are used. We set the initial conditions for the macroscopic velocity field to be zero. In Fig. 4 we show the numerical results of the steady velocity profile and the corresponding analytical solution $v_\theta(r)=[(V_2R_2-V_1R_1)r+R_1R_2(V_1R_2-V_2R_1)/r]/(R_2^2-R_1^2)=0.01(r/30-60/r)$. One can see from Fig. 4 that the agreement with the theoretical results is excellent. The global error was found to be $L_1=1.16\times10^{-5}$.

To illustrate the flexibility of the above FVLBM scheme, we then simulate a two-dimensional Poiseuille flow between two curved plates as shown in Fig. 5. The curved channel has sinusoidal modulation in the top and bottom plates with $y_{\text{bottom}}=A\sin(\pi/2+2\pi x/\lambda)$ and $y_{\text{top}}=L[1+A\sin(3\pi/2+2\pi x/\lambda)]$. Here A is the modulation amplitude, λ is the modulation periodicity, and L is the channel width in the limit of zero amplitude $A=0$. Due to the symmetry of the system, we limit ourselves to the computational domains with one wavelength λ in the x direction. In the simulation we used $\lambda=2L$, $A=0.15$, and $L=32$. The numerical parameters for the FVLBM are $\rho=1.0$, $\tau=0.5$, $\Delta t=0.25$, and $\Delta x=\Delta y=1.0$. The $N_x\times N_y=64\times32$ grids are used. We have set the external body force to $\mathbf{F}=2.604\times10^{-5}\mathbf{e}_x$ so that the maximum velocity for u_x is 0.01 in the case of $A=0$, and the compressibility of the fluid is thus negligible. Since there is no analytical solution for the Poiseuille flow in the curved channel, we have solved the same problem by using the Navier-Stokes equation with the standard marker-and-cell (MAC) method in order to explicitly verify our FVLBM scheme. In Fig. 6 we plot the numerical results of the velocity field from the FVLBM and the numerical solutions from

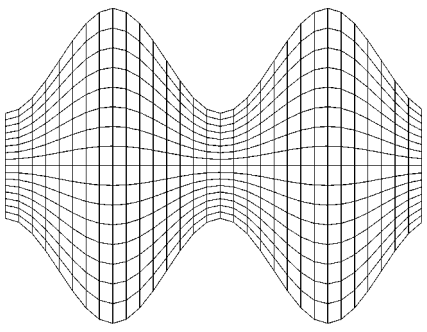

FIG. 5. The quadrilateral meshes used for Poiseuille flow between two curved plates.

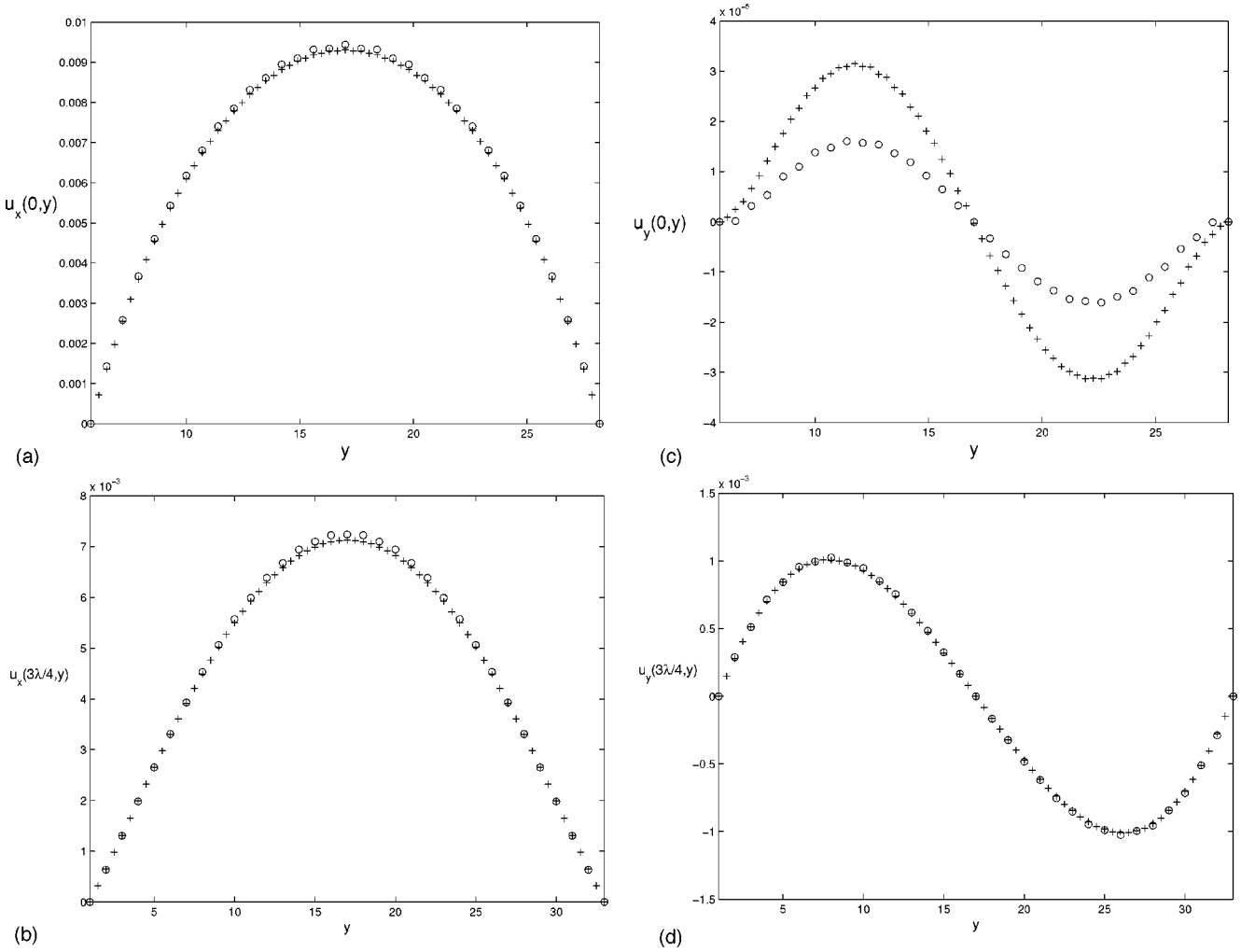

FIG. 6. Velocity profiles in steady state for Poiseuille flow between two curved plates. The x-component velocity was plotted in (a) $u_x(x=0,y)$, (b) $u_x(x=3\lambda/4,y)$, and the y-component velocity was plotted in (c) $u_y(x=0,y)$, (d) $u_y(x=3\lambda/4,y)$. Two sets of symbols stand for finite-volume LBE simulations (circles) and MAC simulations of the Navier-Stokes equation (plus).

the Navier-Stokes equation. Excellent agreement was found as shown in the figures.

We also simulate the two-dimensional problem of plane Couette flow but with a half-cylinder of radius R resting on the bottom plane. The cylinder center is placed in the origin of the coordinates $(x=0,y=0)$. The bottom plane $y=0$ is at rest and the top plane $y=L_y$ moves with uniform velocity $U\hat{e}_x$. The flow field would be $u_x=Uy/L_y$ in the absence of the half-cylinder. The quadrilateral meshes used for the simulation are shown in Fig. 7. The meshes are generated using the usual conformal mapping of complex potential. As in most practices, more grids are placed close to the rigid body since the fluid velocity changes more rapidly near the solid boundary in order for the nonslip condition to be satisfied. In the simulation we use $R=20$ for the radius of cylinder, $U=0.1$ for the top plane speed, and $L_x\times L_y=9.5R\times 6R$ for the physical domain. The numerical parameters for the FVLBM are $\rho=1.0$, $\tau=0.5$, and $\Delta t=0.25$, and $N_x\times N_y=100\times 60$ grids are used. Figure 8 shows the numerical results from the FVLBM and the numerical results by solving the Navier-Stokes equation with the standard finite-element method (FEM). Again excellent agreement was found.

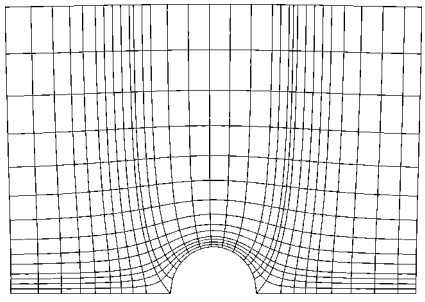

FIG. 7. The quadrilateral meshes used for flow past a half-cylinder resting on a plane.

In three dimensions, we simulated the Taylor-Couette flow where fluid is contained between two concentric long cylinders as shown in Fig. 9. The outer cylinder rotates with a velocity $V\mathbf{e}_\theta$, while the inner cylinder is kept at rest, i.e., $v_\theta(r=R_1,\theta,z)=0$ and $v_\theta(r=R_2,\theta,z)=V$. We set the initial conditions for the macroscopic velocity field to be zero. We have taken the radii of the two cylinders to be $R_1=20$ and $R_2=40$ and the rotating speed of the outer cylinder V to be 0.01. We choose the fluid density $\rho=1.0$ and relaxation time $\tau=1.0$ with external body $\mathbf{F}=\mathbf{0}$. The numerical parameters

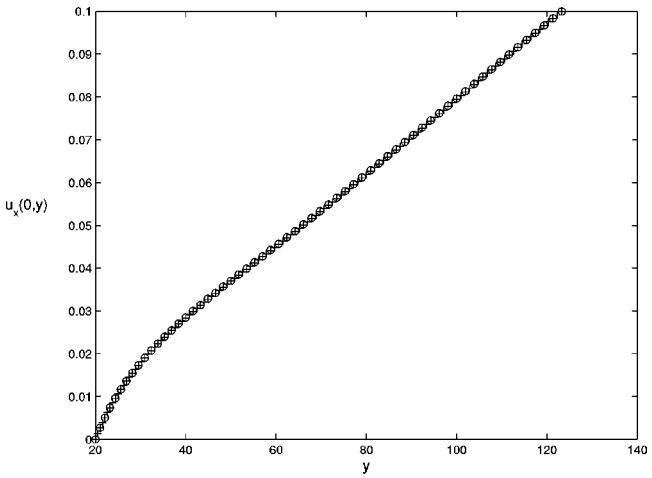

FIG. 8. Velocity field $u_x(x=0,y)$ in the center of the channel is plotted. Two sets of symbols stand for finite volume LBE simulations (circles) and FEM simulations of the Navier-Stokes equation (plus).

for the time and grid step are $\Delta t=0.25$, $\Delta\theta=\pi/45$, $\Delta r=1.0$, and $\Delta z=1.0$. The total of $N_\theta\times N_r\times N_z=90\times 21\times 32$ mesh grids are used. In Fig. 10 we show the numerical results of the steady velocity profile and the corresponding analytical solution $v_\theta(r)=V[R_1R_2/(R_2^2-R_1^2)](r/R_1-R_1/r)$. From Fig. 10 one can see that the agreement with the theoretical results is excellent, and the global error was found to be $L_1=3.26\times 10^{-6}$.

We have also simulated a flow where the inner cylinder moves parallel to its axis with constant velocity $V\mathbf{e}_z$ inside a coaxial cylinder, which is kept at rest, i.e., $v_z(r=R_1,\theta,z)=V$ and $v_z(r,\theta,r=R_2)=0$. Obviously, this is different from Taylor-Couette rotating flow, where the boundary condition is $v_\theta(r=R_1,\theta,z)=0$ and $v_\theta(r=R_2,\theta,z)=V$. In the simulation, the numerical parameters (fluid density, relaxation, time step, etc.) are the same as in the rotating Couette flow. Again, we have compared our numerical results with the analytical solution $v_z(r)=V\ln(r/R_2)/\ln(R_1/R_2)$. In Fig. 11 we show the numerical results and find that they agree extremely well with the theoretical result. The global error was found to be $L_1=4.16\times 10^{-6}$.

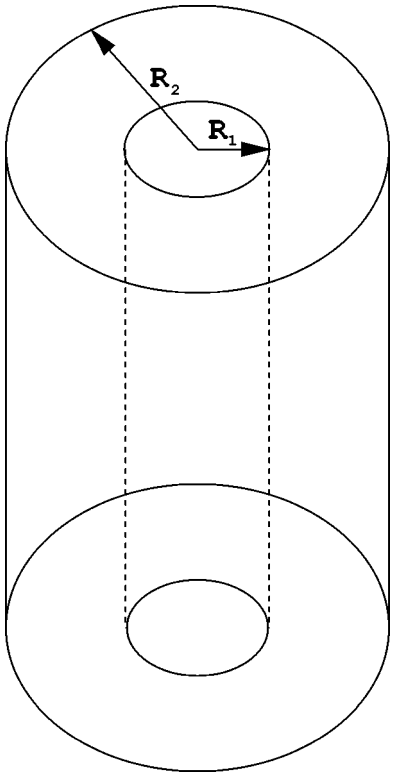

FIG. 9. Scheme diagram for the flow between two concentric cylinders.

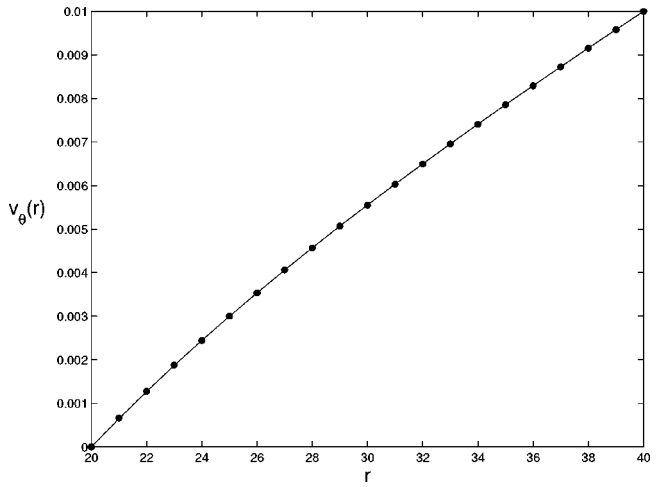

FIG. 10. Numerical velocity profile (data points) in the steady state for rotating Taylor-Couette flow, compared with the analytical solution (solid curve) $v_\theta(r)=V[R_1R_2/(R_2^2-R_1^2)](r/R_1-R_1/r)$.

In the final example, we apply the FVLBM to simulate the Poiseuille flow between the two concentric long cylinders. The flow has the analytical velocity profile between two cylinders,

$$v_z(r)=\frac{F}{4\rho\nu}\left[R_2^2-r^2+\frac{R_2^2-R_1^2}{\ln(R_2/R_1)}\ln\left(\frac{r}{R_2}\right)\right] \qquad (37)$$

for $R_1\leqslant r\leqslant R_2$ with boundary condition $v_z(r=R_1,\theta,z)=v_z(r=R_2,\theta,z)=0$. We choose the fluid density $\rho=1.0$,

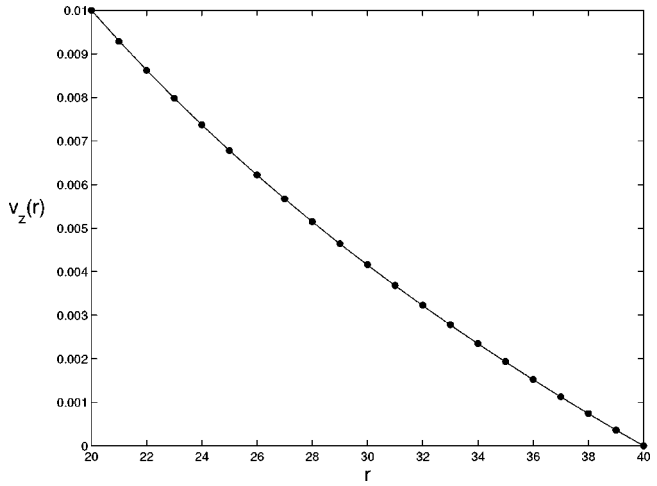

FIG. 11. Numerical velocity profiles in the steady state for the inner cylinder moving parallel to the z axis with constant velocity $V\mathbf{e}_z$ while the outer cylinder kept at rest. The analytical solution is the solid curve $v_z(r)=V\ln(r/R_2)/\ln(R_1/R_2)$.

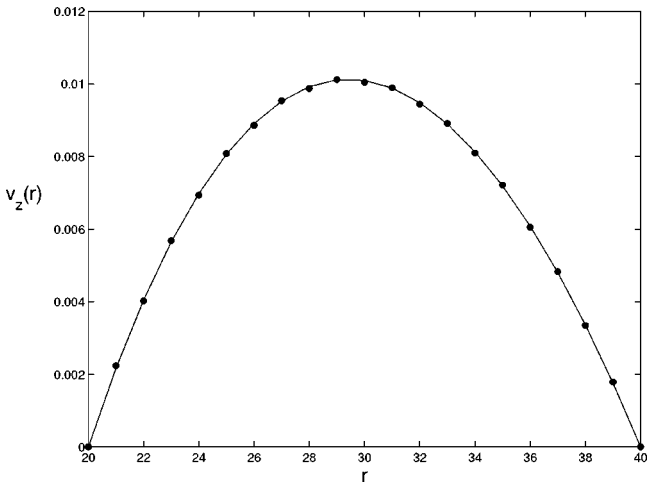

FIG. 12. Numerical velocity profiles in the steady flow for Poiseuille flow between two concentric long cylinders, compared with the analytical solution (solid curve) $v_z(r)=F/(4\rho\nu)\{R_2^2-r^2+[(R_2^2-R_1^2)/\ln(R_2/R_1)]\ln(r/R_2)\}$.

relaxation time $\tau=1.0(\nu=\tau/3)$, and external body force $\mathbf{F}=(20/3)\times10^{-5}\mathbf{e}_z$. The time step and grid step are $\Delta t=0.25$, $\Delta\theta=\pi/45$, $\Delta r=1.0$, and $\Delta z=1.0$. A total of $N_\theta\times N_r\times N_z=90\times21\times32$ mesh grids are used. It is worth emphasizing again that even though the Poiseuille flow problem has high symmetry in velocity field, the FVLBM scheme needs no preassumptions of flow symmetry. The numerical result of Fig. 12 is compared with the theoretical curve. The agreement with the theoretical results is excellent, and global error was found to be $L_1=2.75\times10^{-5}$.

V. CONCLUDING REMARKS

To conclude, we have proposed finite-volume schemes for solving the lattice Boltzmann equation in two and three dimensions. The schemes are flexible and can be applied to unsteady, incompressible fluid flow in a wide variety of regions which contain arbitrarily shaped internal and external boundaries. The schemes involve minimum approximation and do not need to introduce any free parameters. We have not found numerical diffusion problems in our finite-volume schemes. The CFL condition in the current finite-volume scheme is found to be of the form $v_i\Delta tc/h\leqslant1$, where h is a minimum length scale of the control volume and c is a constant depending on the shape of the control volume. The formulation on which our schemes are based does not require a special mesh connectivity. This allows the LBE methods to be applied to many interesting systems that were previously difficult to treat using the conventional LBM, as we illustrated in this paper. Several applications such as turbulent flow near airfoil as well as extensions to thermal problems are under investigation and will be reported in subsequent publications.

ACKNOWLEDGMENTS

This work was supported by PRF under Contract No. 33160-GB9 and the Research Corporation under Grant No. CC4250. The simulations were performed on the SGI Origin 2000 at the Ohio Supercomputer Center. The authors thank Dr. S. A. Ivanenko at the Computing Center of the Russian Academy of Science for helpful discussions.

[1] *Lattice Gas Method for Partial Differential Equations*, edited by G. D. Doolen (Addison-Wesley, Redwood City, CA, 1990); *Lattice Gas Methods: Theory, Applications and Hardware*, edited by G. D. Doolen (MIT, Cambridge, MA, 1991).

[2] R. Benzi, S. Succi, and M. Vergassola, Phys. Rep. **222**, 145 (1992).

[3] J. Stat. Phys. **81** (10) (1995), special issue on lattice-based models and related topics, edited by J. L. Lebowitz, S. A. Orszag, and Y. H. Qian.

[4] S. Chen and G. D. Doolen, Annu. Rev. Fluid Mech. **30**, 329 (1998).

[5] S. Succi, G. Amati, and R. Benzi, J. Stat. Phys. **81**, 5 (1995); F. Nannelli and S. Succi, *ibid.* **68**, 401 (1992); G. Amati, S. Succi, and R. Benzi, Fluid Dyn. Res. **19**, 289 (1997).

[6] H. Chen, Phys. Rev. E **58**, 3955 (1998).

[7] X. He, L.-S. Luo, and M. Dembo, J. Comput. Phys. **129**, 357 (1996).

[8] G. Peng, H. Xi, C. Duncan, and S.-H. Chou, Phys. Rev. E **58**, R4124 (1998); **59**, 4675 (1999); G. Peng, H. Xi, and S.-H Chou, Int. J. Phys. C (to be published).

[9] H. Xi, G. Peng, and S.-H. Chou, Phys. Rev. E **59**, 6202 (1999).

[10] K. W. Morton, *Numerical Solutions of Convection-Diffusion Problems* (Chapman & Hall, London, 1996).

[11] C. Hirsch, *Numerical Computation of Internal and External Flows, Vol. I: Fundamentals of Numerical Discretization* (Wiley, Chichester, 1988).

[12] A. A. Charakhcyan and S. A. Ivanenko, J. Comput. Phys. **136**, 385 (1997).

[13] Harmonic mappings, in *Handbook of Grid Generation* (CRC Press, Boca Raton, FL, in press).

[14] S. Chen, D. Martínez, and R. Mei, Phys. Fluids **8**, 2527 (1996).

[15] N. Cao, S. Chen, S. Jin, and D. Martínez, Phys. Rev. E **55**, R21 (1997).

[16] X. He and L.-S. Luo, Phys. Rev. E **55**, R6333 (1997); **56**, 6811 (1997).

[17] P. L. Bhatnagar, E. P. Gross, and M. Krook, Phys. Rev. **94**, 511 (1954).

[18] Y. H. Qian, D. d'Humieres, and P. Lallemand, Europhys. Lett. **17**, 479 (1992).